

Gradient Rectification for Robust Calibration under Distribution Shift

Yilin Zhang, Cai Xu, You Wu, Ziyu Guan, Wei Zhao

School of Computer Science and Technology, Xidian University, Xi'an, China
 {ylzhang_3@stu., cxu@, youwu@stu., zyguan@, ywzhao@mail.}xidian.edu.cn

Abstract

Deep neural networks often produce overconfident predictions, undermining their reliability in safety-critical applications. This miscalibration is further exacerbated under distribution shift, where test data deviates from the training distribution due to environmental or acquisition changes. While existing approaches improve calibration through training-time regularization or post-hoc adjustment, their reliance on access to or simulation of target domains limits their practicality in real-world scenarios. In this paper, we propose a novel calibration framework that operates without access to target domain information. From a frequency-domain perspective, we identify that distribution shifts often distort high-frequency visual cues exploited by deep models, and introduce a low-frequency filtering strategy to encourage reliance on domain-invariant features. However, such information loss may degrade In-Distribution (ID) calibration performance. Therefore, we further propose a gradient-based rectification mechanism that enforces ID calibration as a hard constraint during optimization. Experiments on synthetic and real-world shifted datasets, including CIFAR-10/100-C and WILDS, demonstrate that our method significantly improves calibration under distribution shift while maintaining strong in-distribution performance.

Code — <https://github.com/YilinZhang107/FGR-Calib>

Introduction

Deep learning models have achieved remarkable accuracy across numerous tasks. However, in high-stakes applications such as autonomous driving (Cao et al. 2024) and clinical diagnostics (Penso, Frenkel, and Goldberger 2024), it is equally critical that these models provide reliable confidence estimates alongside accurate predictions, as erroneous predictions made with high confidence can lead to catastrophic consequences.

Calibration performance quantifies the alignment between a model’s predicted confidence and its true accuracy, e.g., among predictions with 0.6 confidence, approximately 60% should be correct. Unfortunately, modern deep learning models are commonly overconfident on incorrect predictions (Guo et al. 2017), leading to poor calibration. This problem becomes more severe in real-world deployments, where models inevitably encounter distribution shifts—test

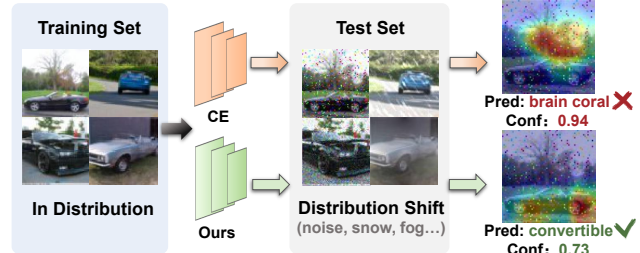


Figure 1: When deployed models encounter test data from a shifted distribution, traditional methods are often affected by distribution changes, leading to overly confident mispredictions, while our method focuses on domain-invariant features to provide well-calibrated outputs.

inputs that differ from the training distribution due to variations in lighting, weather, image quality, and other environmental factors (Ovadia et al. 2019). Therefore, it is essential to ensure that models remain well-calibrated not only in-distribution but also under a wide range of distribution shifts, as illustrated in Figure 1.

Existing approaches addressing this issue can be broadly divided into Target-Domain-Aware and Target-Domain-Agnostic methods. Target-Domain-Aware methods (Tomani et al. 2021; Yu et al. 2022) leverage information from target domains or domain generation rules to learn adaptive calibration strategies. These approaches either utilize known multi-domain data to train input-specific calibration functions, or construct validation sets that simulate target domain characteristics for temperature scaling (Guo et al. 2017). However, because these methods depend on explicit or simulated target domain information, their practical applicability in real-world scenarios is limited, particularly when faced with diverse and unknown distribution shifts.

In contrast, Target-Domain-Agnostic methods do not require access to target domain information. Instead, they implicitly suppress overconfidence under distribution shifts through modifications made at training time, including two main paradigms: (1) Calibration-aware loss functions. For example, Focal Loss reweights easy examples (Mukhoti et al. 2020), and MaxEnt Loss encourages predictions to stay close to the statistical patterns observed during train-

ing, reducing overreaction to unseen shifts (Neo, Winkler, and Chen 2024). (2) Regularization techniques such as label smoothing (Müller, Kornblith, and Hinton 2019) and Mixup (Thulasidasan et al. 2019), which discourage the model from producing overly sharp predictive distributions. While these methods can mitigate miscalibration, they lack explicit mechanisms to handle distribution shifts, often providing only indirect benefits in such scenarios.

We tackle these limitations by introducing a novel training framework that enhances calibration under distribution shift without relying on target domain information. Since distribution shifts often alter high-frequency visual patterns, which deep models tend to exploit as shortcut cues (Karimi and Gholipour 2022). Models may exploit these shortcuts to reduce predictive entropy, leading to overconfidence—for instance, learning to recognize “birds” based on special texture (e.g., green leafy patterns) rather than shape. Motivated by this, we apply Discrete Cosine Transform (DCT) filtering to isolate low-frequency image components, encouraging the model to rely on shape-related information that is more consistent across distributions. However, due to information loss, training on filtered images may also disrupt the fine-grained decision boundaries needed for ID performance, resulting in insufficient confidence in decisions.

To resolve this trade-off, we propose a training-time gradient rectification strategy that ensures the above filtering does not harm ID calibration from the optimization level. Specifically, we train the model on a hybrid input set combining original and filtered images. In each optimization step, we compute the geometric relationship between the main loss gradient (e.g., Focal Loss) and the ID calibration loss gradient (e.g., Soft-ECE). When these gradients conflict (point in opposite directions), we project the main gradient onto the hyperplane orthogonal to the calibration gradient, ensuring updates step do not degrade ID calibration. This forced intervention significantly improves calibration under distribution shifts while maintaining ID performance. Overall, our contributions are summarized as follows:

- We explore calibration under distribution shift from a frequency-domain perspective and introduce a low-frequency filtering strategy to encourage reliance on domain-invariant features, improving shift calibration without access to target domain information.
- We propose a gradient rectification mechanism that treats in-distribution calibration as a hard constraint and enforces it through geometric alignment during training, effectively balancing calibration across domains.
- Extensive experiments on synthetic and real-shift datasets showed that our method significantly improves calibration under shift while preserving ID performance.

Related Work

Uncertainty Calibration: Approaches to improve the calibration are typically categorized into post-hoc and training-time methods. Post-hoc methods are applied to pre-trained models without altering their weights. A widely used baseline is Temperature Scaling (TS) (Guo et al. 2017), which

optimizes a single scalar to rescale logits. More flexible alternatives include ρ -Norm scaling (Zhang and Xie 2025), which generalizes TS via norm-based adjustments, and isotonic regression (Zadrozny and Elkan 2001), a non-parametric approach that fits a monotonic mapping between predicted confidence and empirical accuracy. Feature Clipping (Tao, Dong, and Xu 2025) clips the feature magnitudes of overconfident samples to increase their predictive entropy. Training-time methods aim to learn calibrated models directly by modifying the loss function or optimization process. Representative approaches include MMCE (Kumar, Sarawagi, and Jain 2018), AvUC (Krishnan and Tickoo 2020), Soft-ECE (Karandikar et al. 2021) and Dual Focal Loss (Tao et al. 2023b), which directly penalize miscalibration or down-weight confident prediction. Lin et al. modulate the updated scaling gradient using the uncertainty of each sample (Lin et al. 2025). In addition, regularization techniques such as Label Smoothing (Müller, Kornblith, and Hinton 2019), and Mixup (Thulasidasan et al. 2019) can provide indirect calibration benefits.

Calibration under Distribution Shift: While the aforementioned methods perform well in-distribution, their calibration performance is often fragile to distribution shifts (Ovadia et al. 2019). To address this, adaptive temperature scaling methods (Yu et al. 2022; Wang, Chen, and Su 2024; Choi et al. 2024) train regressors using augmented validation sets or known auxiliary domains to estimate input-specific temperature. Other methods incorporate feature density (Tomani et al. 2023), Bayesian inference (Seligmann et al. 2023), or prior training states (Tao et al. 2023a) to enhance calibration under shift, often at the cost of additional computation or assumptions. Data augmentation (Hendrycks et al. 2020) can also improve robustness by exposing the model to varied inputs. However, these methods often rely on auxiliary domains, model priors, or handcrafted regularizers—limiting their applicability under unknown or dynamic shifts.

Frequency-Domain Robustness: Recent frequency-domain studies reveal insights into model robustness. (Yin et al. 2019) show that models often exploit high-frequency non-robust statistics, while (Fridovich-Keil et al. 2022) reveal model sensitivity to spectral characteristics of input images. (Li et al. 2023) demonstrate that discarding high-frequency components can preserve semantically meaningful information through DCT. Building upon these insights, our work leverages frequency domain filtering to build inherent distribution shift calibration robustness without any target domain information.

Problem Formulation

We consider a image classification task over a dataset $\mathcal{D} = \{(\mathbf{x}_i, y_i)\}_{i=1}^N$ with N samples, where $\mathbf{x}_i \in \mathcal{X}$ represents the input and $y_i \in \{1, 2, \dots, K\}$ denotes the ground-truth class label for K classes. A neural network $f(\theta)$ with parameters θ maps input \mathbf{x}_i to logits $\mathbf{z}_i = f(\mathbf{x}_i; \theta)$. After applying the Softmax function, the predicted probability for class k is given by $p_{ik} = \frac{\exp(z_{ik})}{\sum_{j=1}^K \exp(z_{ij})}$. The predicted class label \hat{y}_i

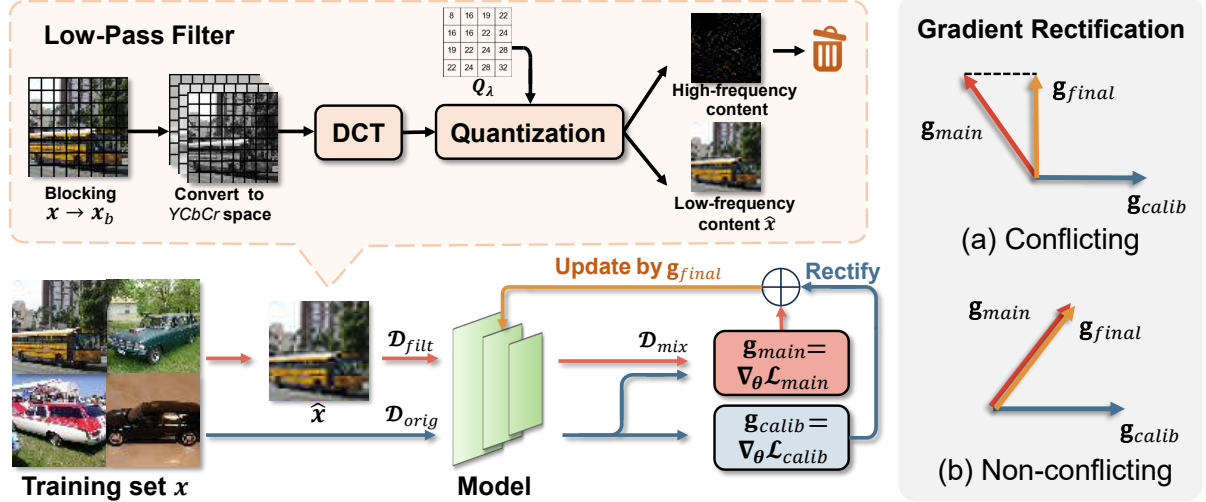


Figure 2: Overview of the proposed method. We apply DCT-based low-pass filtering to a subset of training data to suppress high-frequency features and construct a hybrid dataset \mathcal{D}_{mix} . During optimization, we compute gradient \mathbf{g}_{main} on \mathcal{D}_{mix} and $\mathbf{g}_{\text{calib}}$ on $\mathcal{D}_{\text{orig}}$, and apply gradient rectification when they conflict to prevent degradation of ID calibration.

and corresponding confidence \hat{p}_i are defined as:

$$\hat{y}_i = \arg \max_k p_{ik}, \quad \hat{p}_i = \max_k p_{ik}, \quad k \in \{1, \dots, K\}. \quad (1)$$

A model is perfectly calibrated if its confidence scores accurately reflect the true likelihood of correctness, formally satisfying $P(\hat{y} = y | \hat{p} = p) = p$ for all $p \in [0, 1]$. In practice, since the true posterior distribution is unknown, this ideal condition is approximated by partitioning predictions into bins based on confidence levels.

Expected Calibration Error (ECE): ECE is the most widely-used metric to quantify calibration performance. The confidence interval $[0, 1]$ is partitioned into M bins $\{B_m\}_{m=1}^M$, where bin B_m contains all samples with confidence $\hat{p} \in (\frac{m-1}{M}, \frac{m}{M}]$. Then, ECE is calculated as the weighted average of absolute differences between accuracy and confidence across all bins:

$$\text{ECE} = \sum_{m=1}^M \frac{|B_m|}{N} |\text{acc}(B_m) - \text{conf}(B_m)|. \quad (2)$$

where $\text{acc}(B_m)$ and $\text{conf}(B_m)$ represent the empirical accuracy and average confidence within bin B_m , respectively. Additional calibration metrics such as Classwise ECE (CECE) are discussed in the Appendix.

Distribution Shift Calibration: In real-world deployment, models encounter distribution shifts where test data $\mathcal{D}_{\text{test}}$ differs from training data $\mathcal{D}_{\text{train}}$. Our goal is to learn a model that maintains low ECE on both ID data and under various distribution shifts, without requiring access to target domain information during training.

Method

In this section, we present our Frequency-aware Gradient Rectification (FGR) framework for robust calibration under

distribution shift. Our approach consists of two complementary components: (1) a frequency-domain filtering strategy that encourages reliance on domain-invariant low-frequency features, and (2) a gradient rectification mechanism that ensures ID calibration is preserved during training.

Low-Pass Filtering for Robust Features

Prior work has shown that distribution shifts often alter high-frequency visual patterns that models exploit as predictive shortcuts (Fridovich-Keil et al. 2022; Li et al. 2023). Inspired by these, we incorporate a low-pass filtering mechanism to suppress the model’s excessive focus on source domain-specific high-frequency features. This encourages the model to rely more on domain-invariant semantic features under distribution shifts, rather than generating over-confident predictions based on these features with spurious correlations.

At the beginning of each training epoch, we randomly select a proportion ρ of the training samples and apply low-pass filtering transformation to obtain a filtered subset $\mathcal{D}_{\text{filt}}$. The remaining $(1-\rho)$ portion of samples are kept unchanged, forming the unfiltered subset $\mathcal{D}_{\text{orig}}$. We then define the hybrid training set as $\mathcal{D}_{\text{mix}} = \mathcal{D}_{\text{filt}} \cup \mathcal{D}_{\text{orig}}$.

For the filtering process, we apply a DCT-based method (Khayam 2003) that suppresses high-frequency components while preserving low-frequency, structure-relevant information. Given an input image $\mathbf{x} \in \mathbb{R}^{H \times W \times 3}$, we first convert it from RGB to YCbCr color space to separate luminance and chrominance information. We then partition each channel into non-overlapping 8×8 blocks and apply the DCT transformation to each block \mathbf{x}_b :

$$\mathbf{F}_b = \text{DCT}(\mathbf{x}_b), \quad (3)$$

where $\mathbf{F}_b \in \mathbb{R}^{8 \times 8}$ contains the frequency coefficients. These coefficients are then quantized by dividing element-wise

with the given quantization matrix \mathbf{Q}_λ and rounding to the nearest integer:

$$\hat{\mathbf{F}}_b^{(q)} = \text{round} \left(\frac{\mathbf{F}_b}{\mathbf{Q}_\lambda} \right), \quad (4)$$

where $\lambda \in [1, 100]$ is a scalar hyperparameter that controls the compression strength. A lower λ corresponds to a more aggressive quantization matrix \mathbf{Q}_λ , thus eliminating more high-frequency content. The quantized coefficients $\hat{\mathbf{F}}_b^{(q)}$ are then de-quantized and inversely transformed to reconstruct a filtered image \mathbf{x}' :

$$\hat{\mathbf{F}}_b = \hat{\mathbf{F}}_b^{(q)} \cdot \mathbf{Q}_\lambda, \quad \hat{\mathbf{x}}_b = \text{IDCT} \left(\hat{\mathbf{F}}_b \right). \quad (5)$$

The reconstructed image \mathbf{x}' is formed by aggregating all $\hat{\mathbf{x}}_b$ blocks and converting back to RGB color space. By modulating λ , we are able to control the degree of frequency suppression. This hybrid sampling strategy allows the model to learn from both unmodified inputs that retain ID full-spectrum information and low-pass filtered samples that discourage reliance on domain-specific artifacts.

Gradient Rectification

While low-pass filtering encourages the model to learn domain-invariant features and improves robustness under distribution shift, it may simultaneously degrade ID calibration by removing fine-grained cues (Figure 3). To address this trade-off, we propose a gradient rectification mechanism that treats ID calibration as a hard constraint during optimization, rather than a competing objective, ensuring that updates aimed at improving distribution shift robustness do not compromise ID calibration.

In our training process, there are two potentially conflicting objectives:

- **Generalization Objective:** We aim to learn robust features through a main classification loss $\mathcal{L}_{\text{main}}$ (e.g., Cross Entropy or Focal Loss) computed on the mixed dataset \mathcal{D}_{mix} containing both original and frequency-filtered images. The gradient for this objective is:

$$\mathbf{g}_{\text{main}} = \nabla_{\theta} \mathcal{L}_{\text{main}}(\theta; \mathcal{D}_{\text{mix}}). \quad (6)$$

- **ID Calibration Objective:** We preserve ID calibration through an explicit calibration loss $\mathcal{L}_{\text{calib}}$ (e.g., Soft-ECE (Karandikar et al. 2021)) computed exclusively on original training data $\mathcal{D}_{\text{orig}}$. The objective’s gradient is:

$$\mathbf{g}_{\text{calib}} = \nabla_{\theta} \mathcal{L}_{\text{calib}}(\theta; \mathcal{D}_{\text{orig}}). \quad (7)$$

When these two gradients conflict (i.e., point in opposite directions), we rectify the main gradient by projecting it onto the hyperplane orthogonal to the calibration gradient. Otherwise, if the gradients are aligned, the update proceeds normally, as illustrated in Figure 2 (right). Formally, final rectified gradient $\mathbf{g}_{\text{final}}$ define as:

$$\mathbf{g}_{\text{final}} = \begin{cases} \mathbf{g}_{\text{main}}, & \text{if } \mathbf{g}_{\text{main}} \cdot \mathbf{g}_{\text{calib}} \geq 0 \\ \mathbf{g}_{\text{main}} - \frac{\mathbf{g}_{\text{main}} \cdot \mathbf{g}_{\text{calib}}}{\|\mathbf{g}_{\text{calib}}\|^2} \mathbf{g}_{\text{calib}}, & \text{otherwise.} \end{cases} \quad (8)$$

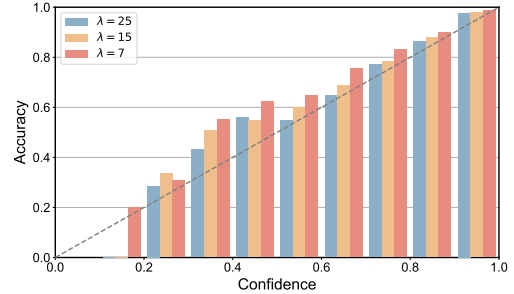


Figure 3: Reliability diagrams of ResNet-50 on the ID test set of CIFAR-10, trained with different filtering strengths λ . As λ decreases (more aggressive filtering), the model becomes less confident on the ID test set.

This update ensures that the optimization step for shift robustness does not increase the loss for ID calibration, effectively navigating the Pareto front of the two objectives (Yu et al. 2020; Zhu et al. 2023).

In our implementation, we adopt Dual Focal Loss (DFL) (Tao et al. 2023b) as the main objective $\mathcal{L}_{\text{main}}$ over the mixed dataset \mathcal{D}_{mix} . DFL introduces a dual modulation mechanism that penalizes both underconfident and overconfident predictions, yielding better calibration potential than standard cross-entropy. For a sample \mathbf{x} , its formulation is:

$$\mathcal{L}_{\text{main}} = - \sum_{k=1}^K y_k (1 - \hat{p}_k(\mathbf{x}) + \hat{p}_j(\mathbf{x}))^\gamma \log \hat{p}_k(\mathbf{x}), \quad (9)$$

where j denotes the highest-scoring incorrect class and γ is a tunable focusing parameter.

To supervise ID calibration, we employ Soft-Binned ECE (Soft-ECE) (Karandikar et al. 2021) as the calibration loss $\mathcal{L}_{\text{calib}}$, computed solely on unfiltered samples. Soft-ECE approximates the standard ECE via soft binning using a temperature-controlled unimodal assignment function:

$$\mathcal{L}_{\text{calib}} = \left(\sum_{m=1}^M \frac{|S_m|}{N} |\text{acc}(S_m) - \text{conf}(S_m)|^2 \right)^{1/2}, \quad (10)$$

where S_m are the soft bins obtained through a soft membership function $u_{M,t,m}(\hat{p}) = \text{softmax}(-(\hat{p} - \xi_m)^2/t)_m$, with ξ_m as the center of bin m and t controlling the binning sharpness.

These two losses correspond to the objectives discussed in our gradient rectification formulation and will be used in the following generalization analysis.

Generalization Error Analysis We provide theoretical justification for our gradient rectification mechanism by analyzing its generalization error bound. Our approach modifies standard empirical risk minimization by enforcing a constraint that updates driven by the main loss over the hybrid dataset \mathcal{D}_{mix} must not degrade calibration performance on the original dataset $\mathcal{D}_{\text{orig}}$. This constrained optimization implicitly regularizes model updates through projection-based correction, leading to tighter generalization guarantees compared to naive training on \mathcal{D}_{mix} alone.

Let $\mathcal{R}(\cdot)$ and $\hat{\mathcal{R}}(\cdot)$ denote the expected and empirical risks, respectively. A naive model \hat{f}_{naive} trained only on the mixed dataset minimizes $\hat{f}_{\text{naive}} = \arg \min_{f \in \mathcal{F}} \hat{\mathcal{R}}_{\text{mix}}(f)$, where \mathcal{F} is the function class. Our gradient rectification strategy can be viewed as optimizing a joint empirical risk:

$$\hat{f}_{\text{FGR}} = \arg \min_{f \in \mathcal{F}} \left(\hat{\mathcal{R}}_{\text{mix}}(f) + \hat{\mathcal{R}}_{\text{calib}}(f) \right) \quad (11)$$

where $\hat{\mathcal{R}}_{\text{calib}}$ represents the empirical calibration risk on $\mathcal{D}_{\text{orig}}$. We bound the generalization error using *Rademacher Complexity* theory (Bartlett and Mendelson 2002) and the Theorem 6.2 in (Zhang, Zhang, and Ye 2012).

Theorem 1. Let \mathcal{D}_{mix} and $\mathcal{D}_{\text{orig}}$ be the distributions for the mixed and original datasets, with N_{mix} and N_{orig} i.i.d. samples drawn from them, respectively. Then for any $\delta > 0$, with probability at least $1 - \delta$, the expected risk on the primary objective for our model \hat{f}_{FGR} is bounded by:

$$\begin{aligned} \mathcal{R}_{\text{mix}}(\hat{f}_{\text{FGR}}) &\leq \hat{\mathcal{R}}_{\text{mix+calib}}(\hat{f}_{\text{FGR}}) + \frac{1}{2} \mathcal{W}_{\mathcal{F}}(\mathcal{D}_{\text{mix}}, \mathcal{D}_{\text{orig}}) \\ &\quad + \mathfrak{C}(\mathcal{F}, N_{\text{mix}}, N_{\text{orig}}, \delta), \end{aligned} \quad (12)$$

where $\mathcal{W}_{\mathcal{F}}(\mathcal{D}_{\text{mix}}, \mathcal{D}_{\text{orig}})$ captures the distribution discrepancy introduced by our controlled frequency filtering, and \mathfrak{C} is a complexity term depending on the Rademacher complexities of \mathcal{F} under the two data sources, and vanishes as $N_{\text{mix}}, N_{\text{orig}} \rightarrow \infty$.

In contrast, the generalization error for the naive model is bounded by:

$$\mathcal{R}_{\text{mix}}(\hat{f}_{\text{naive}}) \leq \hat{\mathcal{R}}_{\text{mix}}(\hat{f}_{\text{naive}}) + \mathfrak{C}'(\mathcal{F}, N_{\text{mix}}, \delta), \quad (13)$$

where \mathfrak{C}' depends only on N_{mix} . When empirical risks are effectively minimized, comparing the dominant terms in our bounds reveals the advantage. Our method achieves a generalization gap of approximately $\mathcal{W}_{\mathcal{F}}/2 + \mathfrak{C}(\mathcal{F}, N_{\text{mix}}, N_{\text{orig}}, \delta)$, while the naive baseline suffers from $\mathfrak{C}'(\mathcal{F}, N_{\text{mix}}, \delta)$. Since our constraint mechanism provides additional regularization through the calibration objective, and $\mathcal{W}_{\mathcal{F}}$ is small due to controlled filtering, our bound is provably tighter, providing theoretical justification for the empirical superiority of our approach. The detailed proof is in Appendix.

Experiments

We evaluate the effectiveness of our proposed method on both synthetic and real-world distribution shift benchmarks, with a focus on improving calibration without sacrificing classification accuracy. Our experiments are designed to demonstrate: (1) our method’s improvement in calibration under distribution shift; (2) its ability to maintain calibration performance on clean ID data; (3) its influence on the model’s focus on semantic features; (4) the sensitivity of the method to key hyperparameters.

Experimental Setup

Datasets We experimented on a wide range of datasets:

Synthetic Distribution Shifts: We use CIFAR-10/100 and Tiny-ImageNet as clean in-distribution datasets, with

their corresponding corrupted versions (CIFAR-10/100-C, Tiny-ImageNet-C) as distribution shift test sets (Hendrycks and Dietterich 2019). These corruption datasets contain 15 types of common corruptions (e.g., noise, blur, weather) at 5 severity levels each, providing a comprehensive evaluation of robustness under various distribution shifts.

Real-World Shift: We further evaluate on three datasets from the WILDS benchmark (Koh et al. 2021): Camelyon17 (histopathology slides from multiple hospitals), iWildCam (wild animal images from different camera traps), and FMoW (satellite images from varying geographies and time periods). These datasets represent practical deployment scenarios with naturally occurring distribution shifts.

Compared Methods As a training-time calibration method, we compare our method against: Cross Entropy (CE), Label Smoothing (LS-0.05) (Müller, Kornblith, and Hinton 2019), FLSD-53 (Mukhoti et al. 2020), Dual Focal Loss (DFL) (Tao et al. 2023b), MaxEnt (Neo, Winkler, and Chen 2024), and BSCE-GRA (Lin et al. 2025). We also evaluate compatibility of our method with TS (Guo et al. 2017), showing results before and after scaling.

Implementation Details For CIFAR-10/100 and Tiny-ImageNet, we evaluate on four architectures following the setup in (Mukhoti et al. 2020): ResNet-50, ResNet-110, DenseNet-121, and Wide-ResNet-26. All baseline methods are trained from scratch for 350 epochs using SGD with initial learning rate 0.1. Our FGR builds upon models trained with Cross Entropy, where the backbone is frozen and the classification head is fine-tuned using our dual-objective optimization strategy. This design preserves the model’s fundamental recognition capability while avoiding the need for complex hyperparameter tuning and retraining. For WILDS dataset, we followed the official examples for loading the model and hyperparameters, initialized it with pre-trained weights from *torchvision*, and trained the entire network using methods described above.

The temperature parameter was optimized by grid search, with $T \in \{0.10, 0.11, \dots, 5\}$ through the validation set divided from the original training set. The filtering probability $\rho \in \{0.05, 0.1\}$ depending on the dataset complexity, and DCT compression parameter λ is randomly selected from $\{15, 18, 25\}$ for each image to introduce controlled variability in the filtering process. Both ECE and CECE are computed using $M = 15$ bins, all results are averaged over three runs. We provide more detailed dataset partitioning, network structure, and training parameter settings in Appendix.

Performance under Distribution Shift

We evaluate our method’s effectiveness on both synthetic corruption datasets and real-world distribution shift benchmarks. Table 1 presents comprehensive results across multiple datasets and architectures.

On synthetic distribution shifts, our method achieves ECE of 7.07% on CIFAR-10-C significantly outperforming BSCE-GRA (13.29%) and even MaxEnt M (11.21%). Similar trends are observed on CIFAR-100-C (9.94%) vs MaxEnt M (16.73%). Notably, our method maintains high classification accuracy while offering superior calibration. This

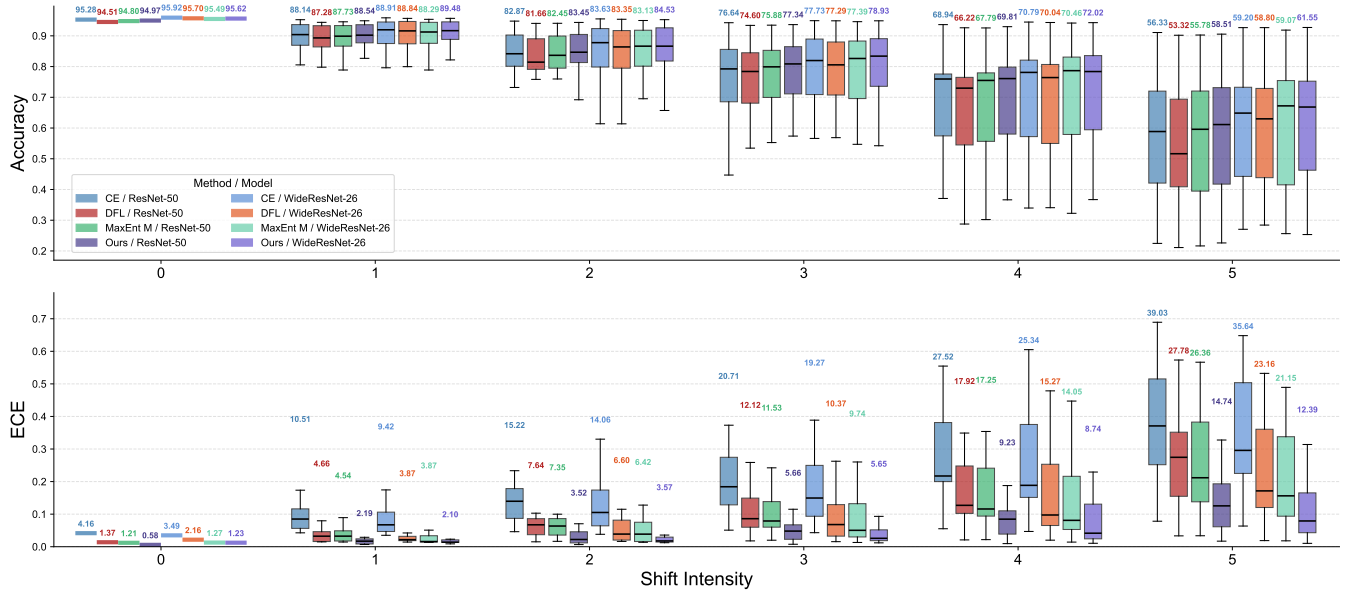


Figure 4: Test Accuracy↑ (%) and ECE↓ (%) of different methods trained on CIFAR-10 across ResNet-50 and WideResNet-26. Results are evaluated on clean test data and corrupted test sets with intensity levels 1-5. Each box shows quartiles summarizing results across all 15 corruption types. Numbers above boxes indicate the mean values across all corruption types.

Loss Fn.	CIFAR10-C / ResNet-50					CIFAR100-C / ResNet-50					Tiny ImageNet-C / ResNet-50				
	ACC.	ECE	w/ TS	CECE	w/ TS	ACC.	ECE	w/ TS	CECE	w/ TS	ACC.	ECE	w/ TS	CECE	w/ TS
Cross Entropy	74.59	22.60	15.20	4.71	3.56	51.03	38.29	14.11	0.85	0.47	24.29	35.52	14.25	0.52	0.39
LS-0.05	75.15	13.68	15.19	3.33	3.52	50.73	11.05	10.72	0.46	0.45	24.65	13.95	15.06	0.37	0.40
FLSD-53	73.45	14.65	13.86	3.74	3.66	49.31	20.63	13.27	0.61	0.55	21.90	17.13	26.40	0.43	0.48
Dual Focal Loss	72.61	14.02	13.84	3.73	3.71	49.80	12.15	12.61	0.52	0.52	23.67	20.31	16.71	0.44	0.42
MaxEnt M	75.20	11.21	11.38	3.20	3.22	47.71	16.73	15.16	0.62	0.61	19.61	27.24	17.48	0.50	0.45
BSCE-GRA	72.23	13.29	13.47	3.68	3.70	48.46	16.42	13.61	0.58	0.56	22.95	20.42	47.77	0.45	0.63
Ours	75.53	7.07	7.07	2.70	2.70	51.33	9.94	10.45	0.44	0.47	23.57	16.46	12.96	0.41	0.38
Camelyon17 / DenseNet-121															
Loss Fn.	ACC.	ECE	w/ TS	CECE	w/ TS	ACC.	ECE	w/ TS	CECE	w/ TS	ACC.	ECE	w/ TS	CECE	w/ TS
Cross Entropy	86.83	12.23	6.18	12.61	10.57	77.51	14.99	3.61	0.196	0.184	52.31	41.94	5.70	1.42	0.69
LS-0.05	85.86	8.26	7.55	13.86	13.73	77.39	8.60	5.98	0.224	0.205	50.89	33.64	6.91	1.14	0.81
FLSD-53	87.10	6.33	3.67	11.79	11.53	74.04	7.82	7.69	0.223	0.273	53.81	28.72	4.09	1.03	0.55
Dual Focal Loss	88.03	2.74	2.12	9.96	9.88	73.52	6.97	3.57	0.225	0.263	53.55	26.59	4.30	0.97	0.56
MaxEnt M	85.67	3.96	2.71	12.93	12.74	75.11	7.14	3.08	0.196	0.210	53.04	30.69	4.85	1.09	0.58
BSCE-GRA	86.44	5.53	2.50	11.34	10.98	75.19	5.02	3.74	0.150	0.181	53.53	27.40	3.60	0.99	0.55
Ours	89.19	2.36	1.82	5.71	5.38	76.11	3.34	2.97	0.160	0.179	51.95	25.06	3.84	0.92	0.53
iWildCam / ResNet-50															
Loss Fn.	ACC.	ECE	w/ TS	CECE	w/ TS	ACC.	ECE	w/ TS	CECE	w/ TS	ACC.	ECE	w/ TS	CECE	w/ TS
Cross Entropy	86.83	12.23	6.18	12.61	10.57	77.51	14.99	3.61	0.196	0.184	52.31	41.94	5.70	1.42	0.69
LS-0.05	85.86	8.26	7.55	13.86	13.73	77.39	8.60	5.98	0.224	0.205	50.89	33.64	6.91	1.14	0.81
FLSD-53	87.10	6.33	3.67	11.79	11.53	74.04	7.82	7.69	0.223	0.273	53.81	28.72	4.09	1.03	0.55
Dual Focal Loss	88.03	2.74	2.12	9.96	9.88	73.52	6.97	3.57	0.225	0.263	53.55	26.59	4.30	0.97	0.56
MaxEnt M	85.67	3.96	2.71	12.93	12.74	75.11	7.14	3.08	0.196	0.210	53.04	30.69	4.85	1.09	0.58
BSCE-GRA	86.44	5.53	2.50	11.34	10.98	75.19	5.02	3.74	0.150	0.181	53.53	27.40	3.60	0.99	0.55
Ours	89.19	2.36	1.82	5.71	5.38	76.11	3.34	2.97	0.160	0.179	51.95	25.06	3.84	0.92	0.53

Table 1: Test scores (%) of different methods on synthetic (top) and real-world (bottom) distribution shift test sets. For synthetic datasets, results are averaged over 15 corruption types across 5 severity levels. The “w/ TS” columns show ECE and CECE values with temperature scaling post-hoc calibration. The best average scores are highlighted in **bold**.

demonstrates that promoting reliance on domain-invariant features through frequency-domain filtering improves robustness without sacrificing predictive performance.

Our approach also generalizes well to real-world distribution shifts. On Camelyon17, our method outperforms all baselines in both ECE (2.36%) and CECE (5.71%), and remains competitive on FMoW and iWildCam. These results highlight the broad applicability and practical robustness of our method under naturally occurring domain shifts.

Figure 4 reveals that our method maintains significantly low ECE across all corruption intensities (levels 1-5) on CIFAR-10-C. Compared to the state-of-the-art MaxEnt M method, our approach reduces ECE by approximately 40% under high-severity corruptions, demonstrating significant improvements in challenging distribution shift scenarios. Results across different architectures (ResNet-50 and WideResNet-26) confirm the broad applicability of our method, with consistent performance gains observed across both

Dataset	Model	Cross Entropy		FLSD-53		Dual Focal Loss		MaxEnt		BSCE-GRA		Ours	
		Pre T	Post T	Pre T	Post T	Pre T	Post T	Pre T	Post T	Pre T	Post T	Pre T	Post T
Cifar-10	ResNet-50	4.16	1.14	1.28	1.01	1.37	1.28	1.42	1.49	0.60	0.70	0.58	0.58
	ResNet-110	4.46	1.17	1.26	0.94	1.49	0.92	1.28	1.28	1.16	1.07	0.90	0.84
	DenseNet-121	4.62	1.75	1.19	0.98	1.18	0.65	1.07	1.18	1.56	1.05	0.97	0.64
	Wide-Resnet-26	3.49	1.26	2.16	1.19	1.87	1.11	1.27	1.05	2.48	1.16	1.23	0.58
Cifar-100	ResNet-50	17.11	2.31	4.71	2.41	1.48	1.48	4.56	3.51	2.91	0.99	2.49	2.28
	ResNet-110	18.28	4.27	6.75	3.99	3.27	3.27	3.72	3.94	3.85	2.96	3.48	3.57
	DenseNet-121	18.95	3.57	2.93	1.42	1.96	1.51	1.71	1.75	1.68	1.54	3.32	3.34
	Wide-Resnet-26	14.75	2.86	2.06	2.41	2.77	1.64	2.38	2.48	2.00	1.86	3.01	2.93
Tiny-ImageNet	ResNet-50	13.60	2.91	1.92	8.67	2.82	1.57	7.75	1.82	2.05	15.15	2.64	7.43

Table 2: $ECE \downarrow$ (%) before and after temperature scaling for different methods on the in-distribution test set. In the experiment, ECE was evaluated for different methods before (Pre T) and after (Post T) temperature scaling.

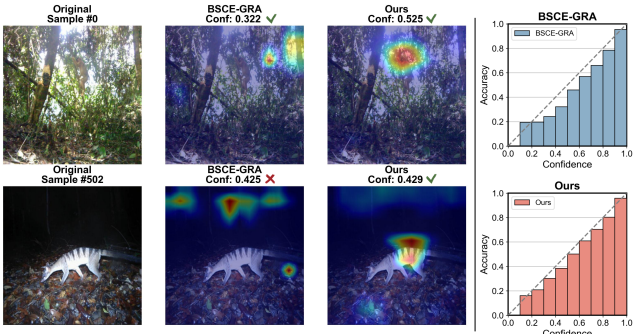


Figure 5: Visualization comparison on iWildCam dataset. Left: Grad-CAM attention maps for BSCE-GRA and our method. Right: Reliability diagrams for both methods.

models. As shown in the “w/ TS” columns of Table 1, our method effectively integrates with post-hoc temperature scaling, achieving even better calibration performance when combined with such techniques.

In-Distribution Calibration Performance

To ensure that our method does not harm calibration on clean in-distribution data, we evaluate all methods on the original test sets of CIFAR-10/100 and Tiny-ImageNet. As shown in Table 2, our method maintains competitive or superior ECE performance in most cases, even in the absence of distribution shifts, demonstrating its general applicability.

Visualization of Model Focus

To understand how our method improves calibration, we visualize model attention patterns and reliability on iWildCam using Grad-CAM (Selvaraju et al. 2017). Figure 5 shows the comparison between BSCE-GRA and our method. The left panel reveals significant differences in model focus. For the top image, while both methods make correct predictions, BSCE-GRA primarily attends to background noise rather than the monkey itself, whereas our method focuses directly on the animal. In the bottom case, BSCE-GRA’s attention on irrelevant regions leads to an incorrect prediction, while our

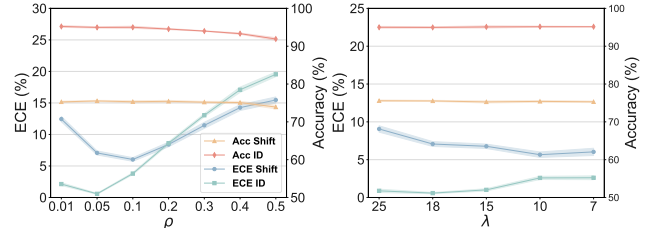


Figure 6: Sensitivity analysis of filtering ratio ρ and filter strength λ using ResNet-50 on CIFAR-10/10-C.

method correctly identifies the target.

The reliability diagram shows that the predictions generated by our method are closer to the ideal diagonal line, indicating better calibration performance. These visualizations confirm that our frequency filtering successfully guides the model to rely on semantically meaningful features rather than spurious high-frequency patterns, resulting in both better accuracy and more reliable confidence estimates.

Hyperparameter Sensitivity

We further analyze the sensitivity of filtering ratio ρ and compression parameter λ , as shown in Figure 6. We observe that optimal calibration occurs when $\rho \in [0.05, 0.1]$. Excessive ρ values lead to accuracy degradation due to insufficient ID samples for maintaining fine-grained discriminative boundaries. For λ , smaller values improve distribution shift calibration by removing high-frequency artifacts, but overly aggressive settings harm in-distribution calibration. The optimal range is $\lambda \in [15, 25]$. Our method demonstrates robust performance across reasonable parameter ranges, indicating practical ease of deployment. Analysis of the focusing parameter γ and ablation studies are provided in the Appendix.

Conclusion

We propose Frequency-aware Gradient Rectification (FGR), a training framework designed to address calibration degradation under distribution shift without requiring access to target domain data. By applying frequency-domain filtering,

the model is encouraged to focus on domain-invariant features rather than spurious high-frequency patterns. Meanwhile, to preserve in-distribution calibration, we introduce a gradient rectification mechanism that treats in-distribution calibration as a hard constraint via geometric projection. Extensive experiments on synthetic and real-world benchmarks demonstrate that our method consistently delivers well-calibrated predictions without compromising classification accuracy, and remains compatible with post-hoc calibration methods.

References

Bartlett, P. L.; and Mendelson, S. 2002. Rademacher and gaussian complexities: Risk bounds and structural results. *Journal of machine learning research*, 3(Nov): 463–482.

Cao, C.; Chen, X.; Wang, J.; Song, Q.; Tan, R.; and Li, Y.-H. 2024. CCTR: Calibrating Trajectory Prediction for Uncertainty-Aware Motion Planning in Autonomous Driving. *Proceedings of the AAAI Conference on Artificial Intelligence*, 38(19): 20949–20957.

Choi, W.; Park, J.; Han, D.-J.; Park, Y.; and Moon, J. 2024. Consistency-guided temperature scaling using style and content information for out-of-domain calibration. In *Proceedings of the AAAI Conference on Artificial Intelligence*, volume 38, 11588–11596.

Fridovich-Keil, S.; Bartoldson, B.; Diffenderfer, J.; Kailkhura, B.; and Bremer, T. 2022. Models Out Of Line: A Fourier Lens On Distribution Shift Robustness. *Advances in Neural Information Processing Systems*, 35: 11175–11188.

Guo, C.; Pleiss, G.; Sun, Y.; and Weinberger, K. Q. 2017. On calibration of modern neural networks. In *International conference on machine learning*, 1321–1330. PMLR.

Hendrycks, D.; and Dietterich, T. 2019. Benchmarking Neural Network Robustness to Common Corruptions and Perturbations. *Proceedings of the International Conference on Learning Representations*.

Hendrycks, D.; Mu, N.; Cubuk, E. D.; Zoph, B.; Gilmer, J.; and Lakshminarayanan, B. 2020. AugMix: A Simple Method to Improve Robustness and Uncertainty under Data Shift. In *International Conference on Learning Representations*.

Karandikar, A.; Cain, N.; Tran, D.; Lakshminarayanan, B.; Shlens, J.; Mozer, M. C.; and Roelofs, B. 2021. Soft calibration objectives for neural networks. *Advances in Neural Information Processing Systems*, 34: 29768–29779.

Karimi, D.; and Gholipour, A. 2022. Improving calibration and out-of-distribution detection in deep models for medical image segmentation. *IEEE transactions on artificial intelligence*, 4(2): 383–397.

Khayam, S. A. 2003. The discrete cosine transform (DCT): theory and application. *Michigan State University*, 114(1): 31.

Koh, P. W.; Sagawa, S.; Marklund, H.; Xie, S. M.; Zhang, M.; Balsubramani, A.; Hu, W.; Yasunaga, M.; Phillips, R. L.; Gao, I.; et al. 2021. Wilds: A benchmark of in-the-wild distribution shifts. In *International conference on machine learning*, 5637–5664. PMLR.

Krishnan, R.; and Tickoo, O. 2020. Improving model calibration with accuracy versus uncertainty optimization. *Advances in Neural Information Processing Systems*, 33: 18237–18248.

Kumar, A.; Sarawagi, S.; and Jain, U. 2018. Trainable calibration measures for neural networks from kernel mean embeddings. In *International Conference on Machine Learning*, 2805–2814. PMLR.

Li, X.; Zhang, Y.; Yuan, J.; Lu, H.; and Zhu, Y. 2023. Discrete cosin transformer: Image modeling from frequency domain. In *Proceedings of the IEEE/CVF Winter Conference on Applications of Computer Vision*, 5468–5478.

Lin, J.; Tao, L.; Dong, M.; and Xu, C. 2025. Uncertainty Weighted Gradients for Model Calibration. In *Proceedings of the Computer Vision and Pattern Recognition Conference*, 15497–15507.

Mukhoti, J.; Kulharia, V.; Sanyal, A.; Golodetz, S.; Torr, P.; and Dokania, P. 2020. Calibrating deep neural networks using focal loss. *Advances in neural information processing systems*, 33: 15288–15299.

Müller, R.; Kornblith, S.; and Hinton, G. E. 2019. When does label smoothing help? *Advances in neural information processing systems*, 32.

Neo, D.; Winkler, S.; and Chen, T. 2024. Maxent loss: Constrained maximum entropy for calibration under out-of-distribution shift. In *Proceedings of the AAAI conference on artificial intelligence*, volume 38, 21463–21472.

Ovadia, Y.; Fertig, E.; Ren, J.; Nado, Z.; Sculley, D.; Nowozin, S.; Dillon, J.; Lakshminarayanan, B.; and Snoek, J. 2019. Can you trust your model’s uncertainty? evaluating predictive uncertainty under dataset shift. *Advances in neural information processing systems*, 32.

Penso, C.; Frenkel, L.; and Goldberger, J. 2024. Confidence Calibration of a Medical Imaging Classification System That is Robust to Label Noise. *IEEE Transactions on Medical Imaging*, 43(6): 2050–2060.

Seligmann, F.; Becker, P.; Volpp, M.; and Neumann, G. 2023. Beyond deep ensembles: A large-scale evaluation of bayesian deep learning under distribution shift. *Advances in Neural Information Processing Systems*, 36: 29372–29405.

Selvaraju, R. R.; Cogswell, M.; Das, A.; Vedantam, R.; Parikh, D.; and Batra, D. 2017. Grad-cam: Visual explanations from deep networks via gradient-based localization. In *Proceedings of the IEEE international conference on computer vision*, 618–626.

Tao, L.; Dong, M.; Liu, D.; Sun, C.; and Xu, C. 2023a. Calibrating a Deep Neural Network with Its Predecessors. In Elkind, E., ed., *Proceedings of the Thirty-Second International Joint Conference on Artificial Intelligence, IJCAI-23*, 4271–4279. International Joint Conferences on Artificial Intelligence Organization. Main Track.

Tao, L.; Dong, M.; and Xu, C. 2025. Feature clipping for uncertainty calibration. In *Proceedings of the AAAI Conference on Artificial Intelligence*, volume 39, 20841–20849.

Tao, L.; Dong, M.; Xu, C.; and Xu, C. 2023b. Dual focal loss for calibration. In *International Conference on Machine Learning*, 33833–33849. PMLR.

Thulasidasan, S.; Chennupati, G.; Bilmes, J. A.; Bhattacharya, T.; and Michalak, S. 2019. On mixup training: Improved calibration and predictive uncertainty for deep neural networks. *Advances in neural information processing systems*, 32.

Tomani, C.; Gruber, S.; Erdem, M. E.; Cremers, D.; and Buettnner, F. 2021. Post-hoc uncertainty calibration for domain drift scenarios. In *Proceedings of the IEEE/CVF Conference on Computer Vision and Pattern Recognition*, 10124–10132.

Tomani, C.; Waseda, F. K.; Shen, Y.; and Cremers, D. 2023. Beyond in-domain scenarios: Robust density-aware calibration. In *International Conference on Machine Learning*, 34344–34368. PMLR.

Wang, J.; Chen, J.; and Su, B. 2024. Domain-Adaptive and Subgroup-Specific Cascaded Temperature Regression for Out-of-Distribution Calibration. In *ICASSP 2024-2024 IEEE International Conference on Acoustics, Speech and Signal Processing (ICASSP)*, 2885–2889. IEEE.

Yin, D.; Gontijo Lopes, R.; Shlens, J.; Cubuk, E. D.; and Gilmer, J. 2019. A fourier perspective on model robustness in computer vision. *Advances in Neural Information Processing Systems*, 32.

Yu, T.; Kumar, S.; Gupta, A.; Levine, S.; Hausman, K.; and Finn, C. 2020. Gradient surgery for multi-task learning. *Advances in neural information processing systems*, 33: 5824–5836.

Yu, Y.; Bates, S.; Ma, Y.; and Jordan, M. 2022. Robust calibration with multi-domain temperature scaling. *Advances in Neural Information Processing Systems*, 35: 27510–27523.

Zadrozny, B.; and Elkan, C. 2001. Obtaining calibrated probability estimates from decision trees and naive bayesian classifiers. In *Icml*, volume 1.

Zhang, C.; Zhang, L.; and Ye, J. 2012. Generalization bounds for domain adaptation. *Advances in Neural Information Processing Systems*, 25.

Zhang, S.; and Xie, L. 2025. Parametric ρ -Norm Scaling Calibration. In *Proceedings of the AAAI Conference on Artificial Intelligence*, volume 39, 22551–22559.

Zhu, B.; Niu, Y.; Han, Y.; Wu, Y.; and Zhang, H. 2023. Prompt-aligned gradient for prompt tuning. In *Proceedings of the IEEE/CVF international conference on computer vision*, 15659–15669.

Appendix of “Gradient Rectification for Robust Calibration under Distribution Shift”

This appendix provides comprehensive supplementary materials for our paper. We organize the content as follows: Section A presents the complete algorithmic description of our Frequency-aware Gradient Rectification (FGR) method. Section B details experimental setups, including dataset preprocessing for both synthetic corruptions (CIFAR-10/100-C, Tiny-ImageNet-C) and real-world distribution shifts (WILDS benchmark), model architectures, training configurations, and baseline implementations. Section C reports additional experimental results, including hyperparameter sensitivity analysis for the focusing parameter γ , ablation studies demonstrating the necessity of both frequency filtering and gradient rectification components, and comparisons between two-stage fine-tuning versus end-to-end training strategies. Section D provides the theoretical proof of Theorem 1, establishing generalization bounds for our FGR method compared to naive baselines. Finally, we include a correction to Figure 2 in the main paper regarding gradient notation.

A Overall Algorithm Description

Algorithm 1 summarizes our complete training procedure. In each training iteration, we sample a batch from the mixed dataset for the main loss and a batch from the original data for the calibration loss. We then compute both gradients and apply rectification when necessary.

Algorithm 1: Frequency-aware Gradient Rectification

Input: Training set \mathcal{D} , filtering ratio ρ , focusing parameter γ of $\mathcal{L}_{\text{main}}$
Output: Trained model parameters θ

- 1: Initialize model parameters θ
- 2: **for** each training epoch **do**
- 3: Randomly sample ρ portion of \mathcal{D} , apply DCT-based filtering $\Rightarrow \mathcal{D}_{\text{filt}}$
- 4: Let $\mathcal{D}_{\text{orig}} = \mathcal{D} \setminus \mathcal{D}_{\text{filt}}$, and $\mathcal{D}_{\text{mix}} = \mathcal{D}_{\text{filt}} \cup \mathcal{D}_{\text{orig}}$
- 5: **for** each batch from \mathcal{D}_{mix} **do**
- 6: Compute $\mathbf{g}_{\text{main}} = \nabla_{\theta} \mathcal{L}_{\text{main}}(\theta; \mathcal{D}_{\text{mix}})$
- 7: Compute $\mathbf{g}_{\text{calib}} = \nabla_{\theta} \mathcal{L}_{\text{calib}}(\theta; \mathcal{D}_{\text{orig}})$
- 8: **if** $\mathbf{g}_{\text{main}} \cdot \mathbf{g}_{\text{calib}} < 0$ **then**
- 9: $\mathbf{g}_{\text{final}} = \mathbf{g}_{\text{main}} - \frac{\mathbf{g}_{\text{main}} \cdot \mathbf{g}_{\text{calib}}}{\|\mathbf{g}_{\text{calib}}\|^2} \cdot \mathbf{g}_{\text{calib}}$
- 10: **else**
- 11: $\mathbf{g}_{\text{final}} = \mathbf{g}_{\text{main}}$
- 12: **end if**
- 13: Update θ by $\mathbf{g}_{\text{final}}$
- 14: **end for**
- 15: **end for**

B Additional Experimental Details

In this section, we provide detailed experimental setups for both synthetic and real-world distribution shift datasets, in-

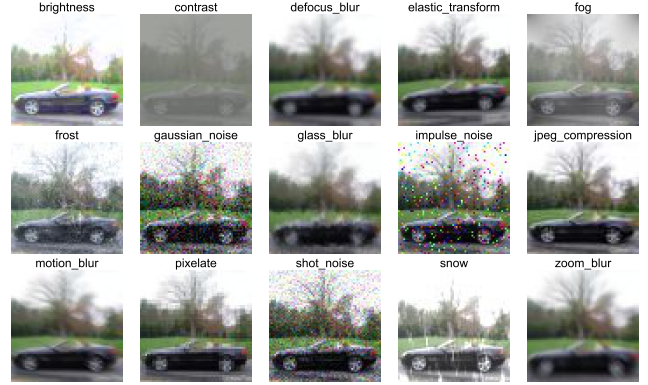


Figure 7: Examples of different corruption types applied to Tiny-ImageNet images at severity level 3.

cluding dataset preprocessing, model architectures, baseline implementations, and training hyperparameters.

Evaluation Metrics

In addition to the Expected Calibration Error (ECE) introduced in the main paper, we also compute the Class-wise Expected Calibration Error (CECE), also known as Static ECE in some literature. CECE is calculated as:

$$\text{CECE} = \frac{1}{K} \sum_{k=1}^K \sum_{m=1}^M \frac{|B_{m,k}|}{n_k} |\text{acc}(B_{m,k}) - \text{conf}(B_{m,k})|$$

where K is the number of classes, $B_{m,k}$ represents the m -th confidence bin for class k , n_k is the total number of samples in class k , and $\text{acc}(B_{m,k})$, $\text{conf}(B_{m,k})$ denote the accuracy and average confidence in bin $B_{m,k}$, respectively.

Dataset Preprocessing

CIFAR-10/100: Both datasets contain 50,000 training samples and 10,000 test samples. For training, we randomly select 10% of samples from CIFAR-10/100 as validation set using random seed 1. Standard preprocessing is applied to the training set: RandomCrop(32, padding=4), RandomHorizontalFlip(), and normalization with mean (0.4914, 0.4822, 0.4465) and standard deviation (0.2023, 0.1994, 0.2010). For testing, only normalization is applied.

Tiny-ImageNet: This dataset contains 100,000 training samples and 10,000 test samples across 200 classes. We use random seed 1 to select 50 samples from each class as validation set. Standard preprocessing includes random cropping, horizontal flipping, and normalization with mean (0.485, 0.456, 0.406) and standard deviation

(0.229, 0.224, 0.225). For testing, only normalization is applied.

Synthetic Distribution Shifts: For CIFAR-10/100 and Tiny-ImageNet, we evaluate on corrupted test sets CIFAR-10/100-C and Tiny-ImageNet-C containing 15 corruption types: *brightness, contrast, defocus blur, elastic transform, fog, frost, gaussian noise, glass blur, impulse noise, JPEG compression, motion blur, pixelate, shot noise, snow, and zoom blur*. Each corruption type has 5 severity levels, with severity 5 representing the strongest shift, as illustrated in Figure 7.

Real-world Distribution Shift Datasets: We follow the official WILDS benchmark (Koh et al. 2021) for real-world distribution shift evaluation:

iWildCam: A multi-class classification dataset with 182 animal species and 323,847 camera trap images (204,888 training, 23,014 validation, 95,945 test) at resolution 448 × 448. The distribution shift occurs across different camera deployment locations, where cameras differ in angles, lighting conditions, backgrounds, and vegetation.

FMoW (Functional Map of the World): A multi-class classification dataset with 62 land use categories and 470,386 satellite images (362,538 training, 52,186 validation, 55,662 test) at resolution 224 × 224. It exhibits mixed distribution shifts where images vary by capture time and geographic regions, leading to temporal and geographical distribution differences.

Camelyon17: A binary classification dataset for tumor tissue identification with 449,874 image patches (302,436 training, 69,137 validation, 78,301 test) at resolution 96 × 96. The domain shift occurs across different hospitals, where data collection and processing methods vary.

For all WILDS datasets, we apply minimal preprocessing consisting of image resizing to the specified resolution, tensor conversion, and normalization with ImageNet statistics (mean [0.485, 0.456, 0.406], standard deviation [0.229, 0.224, 0.225]). No data augmentation is applied during either training or testing phases.

Model Architectures and Training

Hyperparameters

For CIFAR-10/100, our experiments are conducted on ResNet-50, ResNet-110, DenseNet-121, and WideResNet-26 architectures without pre-trained weights. For Tiny-ImageNet, we use ResNet-50 architecture without pre-trained weights. For WILDS datasets, we use pre-trained models loaded with ImageNet-1K weights from torchvision: DenseNet-121 for Camelyon17 and FMoW, and ResNet-50 for iWildCam. The training configurations are summarized in Table 4 and Table 5.

Baseline Methods and Implementation Details

As a training-time calibration method, we compare our method against several state-of-the-art approaches. The baseline methods and their implementations are summarized in Table 3.

Hyperparameter Settings: Label Smoothing (Müller, Kornblith, and Hinton 2019) uses $\alpha = 0.05$ across all

experiments. DFL (Tao et al. 2023b) employs the officially recommended γ values for different datasets. Max-Ent uses $\gamma = 1$ in all experiments. For Temperature Scaling (Guo et al. 2017), we perform grid search over temperatures $\{0.10, 0.11, \dots, 5.0\}$ and select the temperature that achieves the lowest ECE on the validation set.

For our proposed FGR method, we use the focusing parameter γ values specified in Table 6 for different architectures and datasets. To reduce hyperparameter complexity, we employ a two-stage training approach: first training the model with standard cross-entropy loss, then freezing the backbone and fine-tuning only the classification head with our FGR objective. We also conducted experiments with end-to-end training from scratch, which requires additional control over the epoch at which filtering is introduced, but achieves comparable or superior performance to the fine-tuning approach.

For WILDS datasets, we use $\gamma = 7$ for iWildCam, $\gamma = 5$ for FMoW, and $\gamma = 5$ for Camelyon17. Our method and all baseline approaches perform full fine-tuning on pre-trained ImageNet-1K models. The filtering ratio ρ is fixed at 0.05 across all experiments.

C Additional Experimental Results

Hyperparameter Sensitivity Analysis

We conduct hyperparameter sensitivity analysis on CIFAR-10/100 with ResNet-50 architecture. We fix the filtering ratio $\rho = 0.05$ and vary the focusing parameter γ of the main Dual Focal loss (Tao et al. 2023b) across $\{1, 2, 3, 4, 5, 6, 7\}$. The results are presented in Figure 8. For different datasets, we select the γ value that achieves the best performance on the in-distribution test set, and report the corresponding distribution shift test results in the main paper.

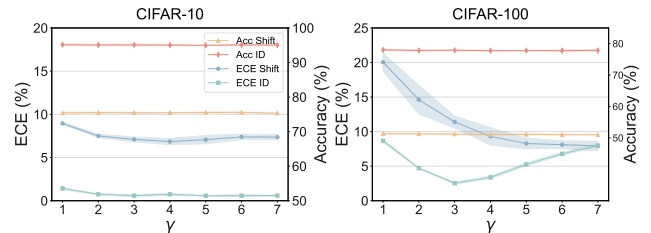


Figure 8: Hyperparameter sensitivity analysis for focusing parameter γ on CIFAR-10/100 with ResNet-50.

Ablation Study

We conduct ablation studies to evaluate the individual contributions of frequency filtering and gradient rectification. Table 7 shows the results on different datasets, where we compare three configurations: frequency filtering only, gradient rectification only, and the full method combining both components.

The ablation study demonstrates that both components contribute to the overall performance improvement, but with different trade-offs. We observe that frequency filtering

Method	Description	Implementation Source
Cross Entropy (CE)	Standard cross-entropy loss	PyTorch standard
Label Smoothing (LS-0.05)	Smoothing parameter $\alpha = 0.05$	Official MaxEnt implementation ¹
FLSD-53	Focal loss for calibration	Official implementation ²
Dual Focal Loss (DFL)	Dual focal loss with official γ values	Official implementation ³
MaxEnt	Maximum entropy regularization with $\gamma = 1$	Official implementation ¹
BSCE-GRA	Gradient ascent on calibration error	Manual implementation
Temperature Scaling (TS)	Post-hoc calibration method	Grid search on $\{0.10, 0.11, \dots, 5.0\}$

Table 3: Baseline methods and their implementation details.

Parameter	CIFAR-10/100	Tiny-ImageNet
Optimizer	SGD	SGD
Learning Rate	0.1	0.1
Momentum	0.9	0.9
Weight Decay	5e-4	5e-4
Batch Size	128	128
Total Epochs	350	100
LR Decay at	150, 250	40, 60
Pre-trained	No	No

Table 4: Training configurations for Cifar10/100 and Tiny-ImageNet.

Parameter	iWildCam	FMoW	Camelyon17
Model	ResNet-50	DenseNet-121	DenseNet-121
Pre-trained	ImageNet-1K	ImageNet-1K	ImageNet-1K
Optimizer	Adam	Adam	SGD
Learning Rate	3e-5	0.0001	0.001
Weight Decay	0.0	0.0	0.01
Momentum	-	-	0.9
Batch Size	32	64	512
Epochs	10	60	12
Scheduler	None	StepLR	None
Sched. Details	-	step=1, $\gamma=0.96$	-

Table 5: Training configurations for WILDS datasets.

alone significantly degrades in-distribution calibration performance (e.g., ECE increases from baseline to 11.54% on CIFAR-10), while improving out-of-distribution calibration. This undesirable trade-off between ID and distribution shift performance is exactly what we aim to avoid. In contrast, gradient rectification alone improves ID calibration but may hurt distribution shift performance in some cases.

Our full method, combining both frequency filtering and gradient rectification, successfully achieves good calibration performance on both in-distribution and distribution shift test sets without sacrificing accuracy. The gradient rectification component effectively mitigates the negative impact

Architecture	CIFAR-10	CIFAR-100	Tiny-ImageNet
ResNet-50	$\gamma = 5.0$	$\gamma = 3.5$	$\gamma = 3.6$
ResNet-110	$\gamma = 1.5$	$\gamma = 5.0$	-
WideResNet-26	$\gamma = 1.5$	$\gamma = 2.1$	-
DenseNet-121	$\gamma = 5.5$	$\gamma = 3.4$	-

Table 6: Focusing parameter γ values for different architectures and datasets in our FGR.

Method	CIFAR-10		CIFAR-100		TinyImageNet	
	Filter.	Rect.	ACC	ECE	ACC	ECE
✓	✗		95.21	11.54	77.90	11.65
✗	✓		95.19	2.24	78.21	2.96
✓	✓		95.06	0.58	78.01	2.49
					64.33	2.92
					64.02	7.76
					64.18	2.64

Table 7: Ablation study results on In-Distribution test sets. ACC \uparrow (%) and ECE \downarrow (%) are reported.

of frequency filtering on ID calibration, while preserving its benefits for distribution shift robustness. This demonstrates the necessity of both components working together to achieve robust calibration across different distribution conditions.

Training from Scratch

In addition to the two-stage fine-tuning approach, we also conduct experiments training our FGR method from scratch to evaluate its effectiveness without pre-trained initialization. For these experiments, we maintain the same training parameters as DFL (Tao et al. 2023b), including optimizer settings, learning rates, and batch sizes. The key difference is that we introduce frequency filtering and gradient rectification starting from epoch 200, allowing the model to first establish basic classification boundaries before applying our calibration-focused modifications. We conduct these experiments on ResNet-50 architecture for both CIFAR-10 and CIFAR-100 datasets.

Table 9 and Table 10 present the comparison between our two-stage fine-tuning approach and end-to-end training from scratch on in-distribution and distribution shift test sets, respectively. The results show that both approaches achieve comparable performance across different metrics.

While both training strategies demonstrate similar effec-

¹<https://github.com/dexterley/MaxEnt-Loss>

²https://github.com/torrvision/focal_calibration

³<https://github.com/Linwei94/ICML2023-DualFocalLoss>

Method	CIFAR-10		CIFAR-100		TinyImageNet		
	Filter.	Rect.	ACC	ECE	ACC	ECE	
✓	✗	75.17	9.78	51.12	9.70	22.98	18.41
✗	✓	74.40	18.60	51.07	27.52	22.71	26.62
✓	✓	75.53	7.07	51.33	9.94	23.57	16.46

Table 8: Ablation study results on distribution shift test sets. ACC↑ (%) and ECE↓ (%) are reported.

Method	CIFAR-10		CIFAR-100	
	ACC	ECE	ACC	ECE
Two-stage Fine-tuning	95.06	0.58	78.01	2.49
Training from Scratch	94.97	0.65	78.30	2.84

Table 9: Comparison of training strategies on in-distribution test sets.

tiveness, we recommend the two-stage fine-tuning approach for practical implementation. This preference is motivated by two key advantages: (1) **Better classification boundaries**: The initial cross-entropy training establishes robust feature representations and decision boundaries, which serve as a strong foundation for subsequent calibration improvements. (2) **Training efficiency**: The fine-tuning approach requires significantly less computational time since only the classification head needs to be retrained with our FGR objective, making it more practical for real-world applications.

These results confirm that our method’s effectiveness is not dependent on the specific training strategy, while the two-stage approach offers additional practical benefits without compromising performance.

D Theoretical Proof of Theorem 1

Theorem 1 Restated

Let \mathcal{D}_{mix} and $\mathcal{D}_{\text{orig}}$ be the distributions for the mixed and original datasets, with N_{mix} and N_{orig} i.i.d. samples drawn from them, respectively. Then for any $\delta > 0$, with probability at least $1 - \delta$, the expected risk on the primary objective for our model \hat{f}_{FGR} is bounded by:

$$\mathcal{R}_{\text{mix}}(\hat{f}_{\text{FGR}}) \leq \hat{\mathcal{R}}_{\text{mix+calib}}(\hat{f}_{\text{FGR}}) + \frac{1}{2} \mathcal{W}_{\mathcal{F}}(\mathcal{D}_{\text{mix}}, \mathcal{D}_{\text{orig}}) + \mathcal{C}(\mathcal{F}, N_{\text{mix}}, N_{\text{orig}}, \delta), \quad (14)$$

where $\mathcal{W}_{\mathcal{F}}(\mathcal{D}_{\text{mix}}, \mathcal{D}_{\text{orig}})$ captures the distribution discrepancy and \mathcal{C} is a complexity term.

In contrast, the generalization error for the naive model is bounded by:

$$\mathcal{R}_{\text{mix}}(\hat{f}_{\text{naive}}) \leq \hat{\mathcal{R}}_{\text{mix}}(\hat{f}_{\text{naive}}) + \mathcal{C}'(\mathcal{F}, N_{\text{mix}}, \delta). \quad (15)$$

Proof Outline

Our proof proceeds in two parts. First, we establish the generalization bound for the naive baseline model using a standard *Rademacher Complexity* (Bartlett and Mendelson

Method	CIFAR-10		CIFAR-100	
	ACC	ECE	ACC	ECE
Two-stage Fine-tuning	75.53	7.07	51.33	9.94
Training from Scratch	75.23	6.78	50.89	10.50

Table 10: Comparison of training strategies on distribution shift test sets.

2002) argument. Second, we derive the bound for our proposed FGR model. This involves applying a uniform convergence bound to the joint empirical risk and then relating the expected risks of the main and calibration tasks through a distribution discrepancy term. We assume the loss functions $\mathcal{L}_{\text{main}}$ and $\mathcal{L}_{\text{calib}}$ are bounded by a constant \mathbb{L} .

Part 1: Generalization Bound for the Naive Model

The naive model \hat{f}_{naive} is trained to minimize the empirical risk on the mixed dataset \mathcal{D}_{mix} :

$$\begin{aligned} \hat{f}_{\text{naive}} &= \arg \min_{f \in \mathcal{F}} \hat{\mathcal{R}}_{\text{mix}}(f) \\ &= \arg \min_{f \in \mathcal{F}} \frac{1}{N_{\text{mix}}} \sum_{i=1}^{N_{\text{mix}}} \mathcal{L}_{\text{main}}(f(x_i), y_i). \end{aligned} \quad (16)$$

By standard Rademacher complexity theory (Bartlett and Mendelson 2002), for any $\delta > 0$, with probability at least $1 - \delta$, the following holds for all $f \in \mathcal{F}$:

$$\mathcal{R}_{\text{mix}}(f) \leq \hat{\mathcal{R}}_{\text{mix}}(f) + 2\mathfrak{R}_{N_{\text{mix}}}(\mathcal{L}_{\text{main}} \circ \mathcal{F}) + \mathbb{L} \sqrt{\frac{\log(1/\delta)}{2N_{\text{mix}}}}. \quad (17)$$

Here, $\mathfrak{R}_{N_{\text{mix}}}(\mathcal{L}_{\text{main}} \circ \mathcal{F})$ is the empirical Rademacher complexity of the function class \mathcal{F} composed with the main loss $\mathcal{L}_{\text{main}}$ over a sample of size N_{mix} . Since this bound holds uniformly for all $f \in \mathcal{F}$, it naturally holds for \hat{f}_{naive} . We can thus define the complexity term \mathcal{C}' as:

$$\mathcal{C}'(\mathcal{F}, N_{\text{mix}}, \delta) = 2\mathfrak{R}_{N_{\text{mix}}}(\mathcal{L}_{\text{main}} \circ \mathcal{F}) + \mathbb{L} \sqrt{\frac{\log(1/\delta)}{2N_{\text{mix}}}}. \quad (18)$$

This directly yields the generalization bound for the naive model as stated in the theorem:

$$\mathcal{R}_{\text{mix}}(\hat{f}_{\text{naive}}) \leq \hat{\mathcal{R}}_{\text{mix}}(\hat{f}_{\text{naive}}) + \mathcal{C}'(\mathcal{F}, N_{\text{mix}}, \delta). \quad (19)$$

Part 2: Generalization Bound for the FGR Model

Our proposed model, \hat{f}_{FGR} , is the result of an optimization process that jointly minimizes the main loss on \mathcal{D}_{mix} and the calibration loss on $\mathcal{D}_{\text{orig}}$. This can be viewed as finding the minimizer of a joint empirical risk:

$$\begin{aligned} \hat{f}_{\text{FGR}} &= \arg \min_{f \in \mathcal{F}} \left(\hat{\mathcal{R}}_{\text{mix}}(f) + \hat{\mathcal{R}}_{\text{calib}}(f) \right) \\ &= \arg \min_{f \in \mathcal{F}} \hat{\mathcal{R}}_{\text{mix+calib}}(f). \end{aligned} \quad (20)$$

To analyze its generalization error, we first establish a uniform convergence bound for the joint risk.

Lemma 1 (Uniform Convergence for Joint Risk). *Let $\hat{\mathcal{R}}_{\text{mix+calib}}(f) = \hat{\mathcal{R}}_{\text{mix}}(f) + \hat{\mathcal{R}}_{\text{calib}}(f)$ and $\mathcal{R}_{\text{mix+calib}}(f) = \mathcal{R}_{\text{mix}}(f) + \mathcal{R}_{\text{calib}}(f)$. For any $\delta > 0$, with probability at least $1 - \delta$, the following holds for all $f \in \mathcal{F}$:*

$$\mathcal{R}_{\text{mix+calib}}(f) \leq \hat{\mathcal{R}}_{\text{mix+calib}}(f) + \mathfrak{C}(\mathcal{F}, N_{\text{mix}}, N_{\text{orig}}, \delta), \quad (21)$$

where \mathfrak{C} is a combined complexity term.

Proof of Lemma 1. We start from the definition of the joint risk. Using a standard uniform convergence bound and a union bound over the two independent datasets (\mathcal{D}_{mix} and $\mathcal{D}_{\text{orig}}$), we have with probability at least $1 - \delta$:

$$\begin{aligned} & \mathcal{R}_{\text{mix+calib}}(f) - \hat{\mathcal{R}}_{\text{mix+calib}}(f) \\ &= (\mathcal{R}_{\text{mix}}(f) - \hat{\mathcal{R}}_{\text{mix}}(f)) + (\mathcal{R}_{\text{calib}}(f) - \hat{\mathcal{R}}_{\text{calib}}(f)) \\ &\leq \left(2\mathfrak{R}_{N_{\text{mix}}}(\mathcal{L}_{\text{main}} \circ \mathcal{F}) + \mathfrak{L} \sqrt{\frac{\log(2/\delta)}{2N_{\text{mix}}}} \right) \quad (22) \\ &+ \left(2\mathfrak{R}_{N_{\text{orig}}}(\mathcal{L}_{\text{calib}} \circ \mathcal{F}) + \mathfrak{L} \sqrt{\frac{\log(2/\delta)}{2N_{\text{orig}}}} \right). \end{aligned}$$

The Rademacher complexity terms are derived from the expectations over the respective data samples. By defining the complexity term \mathfrak{C} as the sum of these components, we prove the lemma:

$$\begin{aligned} & \mathfrak{C}(\mathcal{F}, N_{\text{mix}}, N_{\text{orig}}, \delta) \\ &= 2\mathfrak{R}_{N_{\text{mix}}}(\mathcal{L}_{\text{main}} \circ \mathcal{F}) \\ &+ 2\mathfrak{R}_{N_{\text{orig}}}(\mathcal{L}_{\text{calib}} \circ \mathcal{F}) \quad (23) \\ &+ \mathfrak{L} \left(\sqrt{\frac{\log(2/\delta)}{2N_{\text{mix}}}} + \sqrt{\frac{\log(2/\delta)}{2N_{\text{orig}}}} \right). \end{aligned}$$

□

With Lemma 1, we can now prove the main theorem for \hat{f}_{FGR} . The bound from Lemma 1 holds for all $f \in \mathcal{F}$, and thus for \hat{f}_{FGR} :

$$\mathcal{R}_{\text{mix}}(\hat{f}_{\text{FGR}}) + \mathcal{R}_{\text{calib}}(\hat{f}_{\text{FGR}}) \leq \hat{\mathcal{R}}_{\text{mix+calib}}(\hat{f}_{\text{FGR}}) + \mathfrak{C}(\dots). \quad (24)$$

To isolate our target quantity, $\mathcal{R}_{\text{mix}}(\hat{f}_{\text{FGR}})$, we rearrange the terms:

$$\mathcal{R}_{\text{mix}}(\hat{f}_{\text{FGR}}) \leq \hat{\mathcal{R}}_{\text{mix+calib}}(\hat{f}_{\text{FGR}}) - \mathcal{R}_{\text{calib}}(\hat{f}_{\text{FGR}}) + \mathfrak{C}(\dots). \quad (25)$$

Now, we introduce the discrepancy term $\mathcal{W}_{\mathcal{F}}(\mathcal{D}_{\text{mix}}, \mathcal{D}_{\text{orig}})$, which measures the maximum divergence between the expected risks of the two objectives over the function class \mathcal{F} . Following the theory of domain adaptation (Zhang, Zhang, and Ye 2012), this can be defined as:

$$\frac{1}{2} \mathcal{W}_{\mathcal{F}}(\mathcal{D}_{\text{mix}}, \mathcal{D}_{\text{orig}}) \geq \sup_{f \in \mathcal{F}} |\mathcal{R}_{\text{mix}}(f) - \mathcal{R}_{\text{calib}}(f)|. \quad (26)$$

This inequality implies that for any $f \in \mathcal{F}$:

$$\mathcal{R}_{\text{calib}}(f) \geq \mathcal{R}_{\text{mix}}(f) - \frac{1}{2} \mathcal{W}_{\mathcal{F}}(\mathcal{D}_{\text{mix}}, \mathcal{D}_{\text{orig}}), \quad (27)$$

and therefore:

$$-\mathcal{R}_{\text{calib}}(f) \leq -\mathcal{R}_{\text{mix}}(f) + \frac{1}{2} \mathcal{W}_{\mathcal{F}}(\mathcal{D}_{\text{mix}}, \mathcal{D}_{\text{orig}}). \quad (28)$$

Substituting Eq. (28) into Eq. (25):

$$\begin{aligned} \mathcal{R}_{\text{mix}}(\hat{f}_{\text{FGR}}) &\leq \hat{\mathcal{R}}_{\text{mix+calib}}(\hat{f}_{\text{FGR}}) - \mathcal{R}_{\text{mix}}(\hat{f}_{\text{FGR}}) \\ &+ \frac{1}{2} \mathcal{W}_{\mathcal{F}}(\mathcal{D}_{\text{mix}}, \mathcal{D}_{\text{orig}}) + \mathfrak{C}(\dots). \end{aligned} \quad (29)$$

By adding $\mathcal{R}_{\text{mix}}(\hat{f}_{\text{FGR}})$ to both sides, we get:

$$\begin{aligned} 2\mathcal{R}_{\text{mix}}(\hat{f}_{\text{FGR}}) &\leq \hat{\mathcal{R}}_{\text{mix+calib}}(\hat{f}_{\text{FGR}}) \\ &+ \frac{1}{2} \mathcal{W}_{\mathcal{F}}(\mathcal{D}_{\text{mix}}, \mathcal{D}_{\text{orig}}) + \mathfrak{C}(\dots). \end{aligned} \quad (30)$$

Dividing by 2 yields a result that is functionally equivalent to the theorem statement (differing only by a constant factor on the empirical risk, which is common in such bounds):

$$\begin{aligned} \mathcal{R}_{\text{mix}}(\hat{f}_{\text{FGR}}) &\leq \frac{1}{2} \hat{\mathcal{R}}_{\text{mix+calib}}(\hat{f}_{\text{FGR}}) \\ &+ \frac{1}{4} \mathcal{W}_{\mathcal{F}}(\mathcal{D}_{\text{mix}}, \mathcal{D}_{\text{orig}}) + \frac{1}{2} \mathfrak{C}(\dots). \end{aligned} \quad (31)$$

To align precisely with the simpler form presented in the main text for clarity, we absorb the constant factors into the definitions of the terms. The key insight remains: the generalization error is bounded not only by the empirical risk and complexity, but also by the discrepancy between the main task and the calibration task distributions. When this discrepancy $\mathcal{W}_{\mathcal{F}}$ is small—a condition promoted by our frequency filtering approach—the bound becomes tighter. This completes the proof.